Surface roughness and geological mapping at sub-hectometer scale from the High Resolution Stereo Camera onboard Mars Express

Aurélien Cord [a], David Baratoux [b], Nicolas Mangold [d], Patrick Martin [a], Patrick Pinet [b], Ronald Greeley [c], Francois Costard [d], Philippe Masson [d], Bernard Foing [a], Gerhard Neukum [e]

[a] *European Space Agency (ESA), ESTEC, RSSD, SCI-SB*
Keplerlaan 1, 2201 AZ Noordwijk ZH, The Netherlands

[b] *Observatoire Midi-Pyrénées, UMR5562*
14 av. Edouard Belin, 31400 Toulouse, France

[c] *Department of Geological Sciences, Arizona State University,*
Box 871404, Tempe AZ 85287-1404, USA

[d] *IDES, UMR8148, Bat. 504/509*
Université Paris-Sud, Fac. des sciences, 91405 ORSAY CEDEX, France

[e] *Free University of Berlin, Institute for Geosciences/Planetology,*
Malteserstr. 74-100, D-12249 Berlin, Germany

Preprint submitted to ICARUS *9 February 2007*

Corresponding Author :

Aurélien Cord

14, passage Dubail

75010 PARIS

FRANCE

+33 6 81 70 55 66

FAX : +33 1 64 69 47 07

Aurelien.Cord@cmm.ensmp.fr

Proposed short title :

Surface roughness at sub-hectometer scale from HRSC

Abstract

The quantitative measurement of surface roughness of planetary surfaces at all scales provides insights into geological processes. Complementary of the analysis of local topographic data of the Martian surface at kilometer scale, as achieved from the Mars Orbiter Laser Altimeter (MOLA) data, and at the sub-centimeter scale using photometric properties derived from multi-angular observations, a characterization of roughness variations at the scale of a few tens of meters is proposed. Relying on a Gabor filtering process, an algorithm developed in the context of image classification for the purpose of texture analysis has been adapted to handle data from the High Resolution Stereo Camera (HRSC). The derivation of roughness within a wavelength range of tens of meters, combined with analyses at even longer wavelengths, gives an original view of the Martian surface. The potential of this approach is evaluated for different examples for which the geological processes are identified and the geological units are mapped and characterized in terms of roughness.

Key words: Geological Processes, Impact Processes, Image Processing, Mars Surface, Surface Roughness

Email address: Aurelien.Cord@cmm.ensmp.fr (Aurélien Cord).

1 Introduction

Fluvial, aeolian or glacial activity, impact cratering and landslides are among various geological processes which are responsible for roughness variations on a planetary surface, and particularly on the Martian surface. Such processes control and/or are controlled by grain or rock sizes and their organization on the surface. The quantitative measurement of surface roughness at any scale can provide valuable insights into the characterization of and discrimination between these geological processes. Earlier studies, based on radar and optical determination of Mars surface properties, provided the first measurements of topography variations over scales ranging from centimeters to kilometers. They demonstrated that the physical properties of the Martian surface vary significantly and can be used for understanding surface processes (Simpson et al. 1992, Christensen and Moore 1992). More recent investigations (Kreslavsky and Head 1999, Garvin and Frawley 2000, Kreslavsky and Head 2000, Aharonson et al. 2001, Orosei et al. 2003, Neumann et al. 2003) have produced and analyzed global maps of surface roughness at the sub-kilometer scale or at longer wavelengths. At sub-millimeter to centimeter scales, the surface topography can be investigated by thermal inertia (Putzig et al. 2005, Christensen et al. 2005) and by photometric measurements (Cord et al. 2003, Pinet et al. 2004, 2005a,b,c, Seelos et al. 2005, Shkuratov et al. 2005, Kreslavsky et al. 2006, Johnson et al. 2006). In a study of Gusev crater, the photometric parameters correlate with some geological units present in the crater. They are shown to be very sensitive to particle size (ranging from a few micrometers to a few centimeters) and their organization on the surface (Jehl et al. 2006, Pinet et al. 2006). The quantification of the roughness properties at interme-

diate scales (i.e., tens of meters) is only recently available for the Martian surface by photoclinometry (e. g. Kirk et al. (2003), Beyer et al. (2003)), integrative approach (Golombek et al. 2003) and a two-look roughness algorithm (Mushkin and Gillespie 2005, Adams and Gillespie 2006). We propose in this work a new method to complete this quantification, through the processing of any of the images acquired by high spatial resolution imaging devices onboard current missions (Mars Orbiter Camera / Mars Global Surveyor and HRSC / Mars Express).

For the sake of clarity in the following, we need to distinguish here between *texture* and *roughness*. Following definitions are for use in this paper only. Roughness characterizes the geometric properties of a surface through a quantitative parameter describing the intuitive notions of "rough" or "smooth." The texture quantifies the homogeneous or heterogeneous aspect of an object within an image through digital image analysis, and thus is not a surface property but an image property that relies on the pixel gray-levels in an image. Different sources contribute to the texture in an image, including albedo variations, photometric properties linked to illumination and observation geometries, and the intrinsic roughness of the surface at a scale of several pixels. The main point of the approach detailed below is to enhance the latter contribution and eliminate or reduce the others. As a result, the roughness of geological units can be inferred at a scale of a few tens of meters.

2 Method

In the context of image classification and segmentation, texture content analysis has received much attention during the past decades. Relying on the

comparative study proposed by Randen and Husoy (1999), different filtering methods were tested for the texture characterization of the Martian surface, based on high-resolution images. In the work presented by Cord et al. (2005), 37 images of 256x256 pixels are extracted from the HRSC database. Those images, presented in Figure 1, are selected to exhibit texture properties that are similar within an image. They are sorted into 5 classes, in regard of their visual properties. Using different sets of parameters, the texture properties are evaluated for all those images. They are automatically classified into 5 clusters according to their texture properties, by means of an unsupervised clustering method relying on an EM algorithm (Expectation - Maximization algorithm). The classification, shown in Figure 1, is the closest to the expected one. It corresponds to the Gabor filters and the associated parameter set used in the following steps. This filtering approach is both very efficient in terms of discrimination between texture properties, and easy to implement. Moreover, the possibility of studying the directionality, in particular for geologic features that are not isotropic (e.g. crater ejecta), is kept in mind for the future.

The processing steps (Fig. 2) are described in detail in the following subsections and illustrated using the same scene extracted from the HRSC database (a crater centered at 16.3^o N, 280.8^o E and its surroundings). The geology of this area is given in section 3.3. The corresponding image before any processing is presented in Figure 3a. It is geometrically corrected and projected onto the Digital Elevation Model (DEM) produced using HRSC data ("level 4" data).

To reduce the contribution from surface albedo in the roughness evaluation, we consider large surfaces that exhibit homogeneous albedo and assume that: (1) in a high-resolution image, albedo variations within a given geological unit (e.g., bright versus dark terrain) have a spatial frequency that is smaller than the roughness frequency, (2) the roughness induces some high spatial frequency signal inside a geological unit and the texture is characterized by radiance changes among neighboring pixels, and (3) images of two surfaces having the same roughness but different albedo have relative radiance variations that are proportional to the mean surface albedo. Areas where these assumptions are violated should be interpreted with caution.

Using radiometric calibration, the data is converted into radiance units. In order to eliminate the low-spatial-frequency signal coming from albedo variations, and thus to enhance the high-frequency signal coming from roughness, a high-pass filter is applied: each pixel is divided by a mean DN value of its 51x51 pixel neighborhood. A comparison between Figures 3a and 3b shows that the variation in albedo between the various geological units is removed as expected. Another illustration of this is shown by the top and middle curves in Figure 5.

Gabor filters are first suggested for texture description by Jain and Farrokhnia (1991). The impulse response $h(x, y)$ can be written:

$$h(x,y) = \frac{1}{2\pi\sigma_g^2} e^{-\frac{x^2+y^2}{2\sigma_g^2}} e^{-2\pi j \frac{(x\cos(\alpha)+y\sin(\alpha))}{p_0}}. \quad (1)$$

It corresponds to a sinusoid with a period p_0 and an orientation controlled by α that is modulated by a Gaussian envelope with a scale controlled by the standard deviation σ_g.

The Gaussian envelope is the same for all filters: the size of the filters is 29x29 pixels, σ_g is 0.8x29 pixel. Four orientations ($\alpha \in [0^o, 45^o, 90^o, 135^o]$ with respect to the abscissa axis taken as a reference) and three periods characterizing the spatial scales related to 9, 7 and 4 pixels ($p_0 \in [9, 7, 4]$ $pixels$) are selected.

2.3 Local texture estimate

In the next processing step, a local texture estimate is calculated for the purpose of transforming the filtered areas for which band-pass frequency components are strong into a high-constant gray level, and areas for which these components are weak into a low-constant gray level. The filtered response is rectified (operation of transforming negative amplitudes into the corresponding positive amplitudes) and smoothed (Weszka et al. 1976).

First, we calculate the magnitude of the outputs from the convolution at all periods ($[9, 7, 4]$ $pixels$) and orientations ($[0^o, 45^o, 90^o, 135^o]$). The results obtained with the 9-pixel scale for the four directions are presented in Figure 4. In order to obtain a local texture estimate regardless of the directionality,

the average magnitude based on the orientations is calculated for each value of the period. Then a low-pass Gaussian filter is applied and for this purpose we choose a 29x29 pixel filter with a scale parameter (σ_g) of 0.8x29 pixels.

Figure 5 illustrates all steps of the Gabor filtering process described above. The highest spatial frequencies (see for example the top curve value around pixel number 600 in Figure 5) correspond to the highest values of the local texture (bottom curve). To evaluate the consequences of the reflectance variations induced by the topography along the profile, it is best to focus on the center of the impact crater (pixel numbers from 600 to 1300, in Figure 5). The reflectance values (top curve) have important low-spatial-frequency variations that are corrected by the preprocessing step (middle curve) and thus do not affect texture estimates (bottom curve) that are fairly stable in this part of the profile.

The results obtained so far and named hereafter the *textural image* are qualitatively consistent with the apparent levels of texture for different units within the image and reveal the boundaries between them. The first part of the method can be applied up to this point if the comparison between various locations on the Martian surface is not required.

2.4 From texture to roughness

The objective of this section is to be able to compare textural images of various areas of the surface of Mars that were potentially acquired under different conditions of observations. It requires the conversion of textural image values into a quantity which is independent of illumination and observing geometry.

In order to obtain such a calibration, we have estimated the texture properties of synthetic images using the same filtering sequence. The synthetic images are shaded-relief images from randomly-generated topographic surfaces. Thus, the texture properties can be linked to the topographic characteristics.

2.4.1 Synthetic textures

Topographic surfaces are generated as random self-affine surfaces. The power spectrum of the topography, defined as the square of the coefficients in a Fourier series, has a power law dependence:

$$|F(l)|^2 \propto |l|^{\beta} \tag{2}$$

where F is the Fourier transform of a function representing the elevations, l the wave number, and β the exponent of the power law. The topographic surfaces of Venus, Mars, Earth and the Moon all display an exponent value close to 2 at wavelengths greater than a few kilometers (Balmino 1993, Turcotte 1987). This exponent value corresponds to a Brown noise which is explained in the case of diffusion processes.

However, at shorter wavelengths there is a tendency toward relatively steeper slopes or higher values of β (Dodds and Rothman 2000, Weeks et al. 1996). Here, we assume that the power law with one unique value of the exponent is valid for the restricted range of scales affecting the textural images obtained at one given period. Different values of this exponent likely correspond to different geological processes. In this study, the observation angles are systematically neglected because the images of highest resolution are taken under nadir conditions (the emergence angle is always smaller than 15 degrees). In order

to produce the relationship of β as a function of the texture estimate (i.e., the normogram), the following procedure is repeated ten times and results are averaged for each considered incidence angle.

Digital Elevation Models (DEMs) of 1000 by 1000 pixels are generated in the Fourier space using the power and exponent values ranging from 2 to 9. The phase corresponding to each wave number is generated randomly. The surface topography is thus obtained by inverse Fourier transform. Three examples of the surface generated by this method are given for the exponent values equal to 3, 5 and 9 in Figure 6, along with the corresponding shaded-relief images . Shaded-relief images are computed for each DEM and incidence angle, with the assumption that the maximum slopes never exceed 30^o. The filtering process is applied to the shaded-relief image in the same way as described above to produce synthetic textural images. The mean value of the synthetic textural images is computed and associated to the corresponding exponent value to form the normogram.

Shadows are not considered during the generation of the shaded-relief images. First, even if shadows are an important aspect of the photometric modelling of the sub-pixel surface roughness (e.g., the roughness parameter in the Hapke equation), the contribution of shadows at the scale of this study is considered negligible. Then, as explained in the following, relative roughness values are derived. The potential contribution of shadows would affect the normogram in a monotonic manner. We assume that the second order monotonic contribution can be linearized for the range of incidence angle and surface roughness considered here:

$$G.R._{.withshadow} = a + b * G.R._{.withoutshadow} \tag{3}$$

where G.R. is the response of the image to the Gabor filtering sequence. In that case, relative estimation of roughness remains valid, even if shadows were neglected during the process. Because of this assumption, large wall slopes, or large topographic variations should not be considered by this texture-to-roughness conversion.

Free parameters exist in the process: the amplitude of the first component of the spectrum, and the DN amplitudes of the shaded-relief image. It would have been necessary to introduce a full physical model with the knowledge of surface albedo, surface scattering properties and instrument calibration in order to link textural image values to absolute values of β. The process is only aimed at deriving a corrected value that is independent of the incidence angle. For this purpose, the free parameters must remain constant (first component = 1 and DN amplitude = 255). Finally, we translate the exponent into an equivalent Root Mean Square Slope value (RMSS), as this is a more commonly used notion in planetary science.

2.4.2 Root Mean Square Slope images

There is a bijection between RMSS values computed at a given scale and β, meaning that each value of β corresponds to one and only one RMSS value. The RMSS value is calculated by filtering the surface with a high-pass filter, through a subtraction by a smoothing filter the size of 10x10 pixels (the size of this filter is not crucial because the RMSS will be normalized in the following):

$$RMSS = C * \sqrt{\frac{1}{N} \sum X^2} \tag{4}$$

with N the number of pixels and X corresponding to the difference between the DEM and the low-pass filtered DEM. C is a constant for the normalization

of the RMSS. We choose C ($= 10^3$) to force RMSS to be equal to unity within the ejecta of the impact crater taken as example (Fig. 3a) for the spatial period associated with the 4-pixel scale (Fig. 7). We then obtain as final result the RMSS image or model roughness map.

The RMSS value should thus be understood as a relative measure of the true surface roughness, meaning that a one-to-one correlation exists between our measure and the true surface roughness. But what matters here the most is that RMSS maps should be independent of the incidence angle.

2.4.3 Sensitivity analysis of the method

The effect of the assumptions we used in this approach on the final product cannot be a-priori estimated. We tested the sensitivity of the method by comparing textural values from images of the same area under different conditions of illumination and observation. The two HRSC images were acquired during Mars Express orbits 1210 and 1221 at illumination angles of 29^o and 20^o and of emergence angles of 12^o and 10^o, respectively; the spatial resolution is 13m/pixel in both cases. Figure 8 shows the differences between the two overlapping textural images and the two overlapping RMSS images, expressed in percentage of difference ($100(V1 - V2)/V1$ V1 and V2 are respectively the Digital Number of the first and second image). The mean values for the whole area and for all spatial periods are in table 1. From these results, it appears as expected that the texture properties are highly influenced by illumination conditions (incidence, azimuth). This effect is significantly reduced after filtering and the RMSS values appear much less dependent on the incidence. This example demonstrates that even with a small angular difference, the texture

properties are significantly different while the RMSS values are very similar for the scene. This approach has not been tested for largely different illumination conditions and consequently such situations should be approached carefully.

2.5 Synthesis

In summary, our method provides a quantified estimate of the intrinsic local surface roughness, using calibrated high-resolution images and taking into account the surface albedo and illumination and observing geometries. Except when clouds are present (such cases are to be avoided in surface roughness studies), the atmosphere can be considered homogeneous. Thus, the atmospheric opacity will mainly affect the contrast of the images, and will be eliminated during the preprocessing step.

The HRSC technical data assume a global signal-to-noise ratio (SNR) higher than 100 for panchromatic lines. Since the Gaussian envelope size of Gabor filters is 29x29 pixels, those filters effectively suppress the highest spatial frequencies and hence suppress a large part of the noise. However, if one deals with lower SNR data, in particular if the additive components of the noise (e.g. thermal noise, quantization ?) are important, some noise can be translated into the roughness map after the preprocessing. As an example, if brighter and darker surfaces have the same real surface roughness, the processing output will provide with a lower roughness estimate for brighter areas due to the noise. This additional noise will not necessarily correlate with the geological units. As a consequence, the potential presence of texture units which are apparently decorrelated from the ubiquitous geological units seen on a given image would suggest a dominant noise effect and should call for suspicion.

One must bear in mind that the high RMSS values associated with image edges may result from an edge effect caused by the Gabor filtering and thus have no physical meaning. Indeed, some leakage of the albedo signal into roughness estimates is still possible for areas which have strong, high-frequency albedo variations. Interpretation of roughness estimates should be avoided or conducted with caution in such areas.

This method could be adapted for roughness estimations with other high-resolution images (e.g. MOC). That implies to produce normograms to evaluate the roughness obtained at various scales. To compare the results between them, it may then be worth degrading the spatial resolution of images acquired at high resolution.

3 Application to geological investigations

This section presents a few examples for which the characterization of the roughness provides insight into Martian surface geology. The roughness maps are compiled into RGB composites using the three roughness images of different periods (9, 7 and 4 pixels). The roughness increases from light to dark: i.e., the lighter the image, the smoother the surface. Bluish color indicates a higher roughness at large scale and reddish color indicates a higher roughness at small scale.

3.1 Lobate ejecta craters

Some Martian craters are surrounded by a continuous lobate ejecta blanket for which the emplacement origin is debated (see, Baratoux et al. (2005) and

references therein). Two main processes have been invoked: (1) interaction of ejecta with the atmosphere and winds generated during the impact (Schultz and Gault 1979, Schultz 1992), or (2) surface flow of ejecta fluidized by melting of the sub-surface ice (Carr et al. 1977, Costard 1989). Theoretically, the roughness of the ejecta blanket resulting from surface flow with possible sorting of granular material will be different from the roughness resulting from scouring, transport and deposition of the fine fraction, with coarser fraction left behind when atmospheric processes are dominant (Barnouin-Jha and Schultz 1996, Baratoux et al. 2005). Many surface-modifying processes exist on Mars (wind erosion, dust mantling, ice sublimation, etc.) that can modify the roughness of ejecta through time and therefore must be taken in account.

Figure 9a shows an HRSC image of Chryse Planitia and six impact craters with diameters ranging from 7 to 13 km. Lobate ejecta deposits from these craters have very different texture properties (Fig. 9b) and there is no systematic correlation between the crater diameters and the texture, suggesting no increase in roughness with crater size. Assuming that the states of roughness of the ejecta are similar at the time of crater formation, we plot roughness estimates associated with different spatial periods for the craters and the smooth plains surrounding the craters. The top-right corner in the diagram of Figure 9c corresponds to the roughest terrains, whereas the lower-left corner, closer to the origin, corresponds to the smoothest terrains. Ejecta roughness decreases from crater 1 to crater 6, the latter being close to the mean value of the background. Thus, we interpret this variation in roughness as the result of a progressive degradation of the ejecta by dust mantling and/or wind erosion. Assuming that these processes are homogeneous in this area, it is likely that the decrease in roughness corresponds to an increase in age of the crater. The

older the crater is, the more degraded it becomes. Thus, this example shows that the variations in roughness might be used to assess the relative age of craters, a piece of information difficult to access from crater counting on such a small surface.

Other HRSC images are used to observe crater ejecta in more detail (Fig. 10). The first one (Fig. 10a) has a high roughness, especially at small scale. The second example (Fig. 10b) indicates high small-scale roughness (blue) but also a brown color at the northern edge similar to the roughest ejecta of Figure 9b. In the third example (Fig. 10c), different units can be distinguished based on the roughness map. Note that the center of the crater has the same roughness property as the ejecta. A common characteristic of the crater ejecta is their homogeneous roughness. It is noteworthy that all are in the 45^o mid-latitude region and are similarly affected there by degradation from dust/ice deposition and ice sublimation (Mustard et al. 2001). Pitted terrains are especially visible on the HRSC image in Fig. 10c. Thus, we may suppose that the roughness is closely linked with this degradation process. If it is true, it could explain that the roughness is similar inside the crater and within the ejecta.

The examples of roughness of ejecta deposits described above suggest the following: (i) the roughness of the ejecta appears to result from degradation and is not a primary characteristic of fresh ejecta, (ii) only fresh craters might have roughness characteristics directly related to the impact process, (iii) a regional differential roughness of the ejecta might be used to determine the relative ages of the craters, and (iv) in some cases, roughness might provide insight into specific degradation processes.

Wind streaks are bright or dark albedo patterns that are often associated with craters or other topographic features. They are associated with zones of erosion and deposition induced by wind flows around these obstacles (Sagan et al. 1973, Greeley and Ivsersen 1985, Tanaka et al. 1992). Most bright streaks are thought to be deposits of dust in a "shadow zone" characterized by lower wind speeds. They are thus composed mainly of small-size grains, which could create a very thin layer (lesser than 1mm) (Pelkey et al. 2001). Such a layer does not affect the roughness of the surface, as demonstrated in Figure 9b. The HRSC image of this figure displays many wind streaks which do not appear on the roughness map, implying that the thickness of wind streaks is small enough not to affect the roughness at the scale of the measurement (few tens of meters).

Figure 11 shows examples of wind streaks visible on a roughness map. In Figure 11a, a 15-km diameter crater exhibits a large wind streak. We checked that the smoothest, brightest area in the roughness map is not the result of receiver saturation. It is located on the central part of the large wind streak observed in the visible image. Thus, only part of the wind streak displays a specific roughness that is different from the background. A similar observation can be made for the two regions displayed in Figure 11b and 11c. Wind streaks often stretch for many kilometers long, but are found to be shorter on the roughness map, with smoother roughness being immediately in the lee of the crater. This is consistent with the expected thinning of the deposit with increasing distance from the crater.

Different remarks can be drawn from these observations. First, an assumption of our approach is that there are low-albedo variations within a geological area of the observed surface (at the scale of tens of meters). If this is true, texture variations within the image correspond to roughness variations on the ground. This assumption is not systematically valid, in particular for the dune field in Figure 11a for which RMSS values are very high and meaningless. Then, texture and albedo are not directly correlated: the whole bright albedo of the streak does not correspond to the entire area of smooth texture. Part of the wind streak shows the same roughness than the surrounding plain, which is consistent with the presence of a very thin layer of dust which changes the albedo but not the roughness. Smaller roughness values correspond to a smoothing induced by the aeolian patterns. This shows that there is a relation between RMSS values and the thickness of the dust mantling smoothing an initially rougher surface. Finally, the smoothing is more important closer to the crater rim, demonstrating the existence of a gradient in dust thickness from the crater rim to the more distant part of the ejecta blanket where the roughness of the plain is not modified.

We may expect qualitatively that roughness at the 40-meter scale would require a thickness of material of a few meters to smooth the surface enough to be detected. Indeed, initial roughness of the ejecta considered here are similar and relatively high at this scale in comparison with the surrounding. The effect would not be visible until the dust thickness is sufficiently large compared to the surface RMS slope. This explains why some wind streaks are not visible in the roughness map (Fig. 9b). However, as in Figure 11, when some wind streaks are visible in the roughness map in comparison with other parts of the ejecta, the thickness of the deposit needed to produce this smoothing can be

evaluated to a few meters. Accurate estimation would require a complete modeling such as done by Forsberg-Taylor et al. (2004). Nevertheless, this result suggests that the wind streaks consist of thicker dust deposits than previously supposed, raising the possibility that these streaks formed over long geologic periods without marked directional changes in the prevailing wind pattern.

The observation of the roughness of wind streaks thus leads to interesting conclusions about the formation of these features: (i) some wind streaks are not visible in the roughness map, suggesting a very thin accumulation, whereas others are detected involving the accumulation of meters of dust. (ii) The entire streaks seen in the visible image are not seen in the roughness map, suggesting a gradient in the accumulation of dust from the crater rim to more distant terrains. (iii) The thickness inferred for the smoothing of the terrains suggests that wind streaks result from long-term prevailing wind orientations.

3.3 Lava flows and geological mapping

A region of the northern hemisphere was chosen, based on its different geological units and landforms that can be studied and may have different physical properties (Fig. 12). The geologic map of Scott and Tanaka (1986) shows that the area is at the junction between the Late Hesperian outflow channel of Kasei Valles and Amazonian lava flows originating from the Tharsis plateau. The HRSC image shows overlapping lobate lava flows that have prominent south-eastern slopes. This is confirmed by MOLA topography which shows a South-East-oriented gradual slope, to the West of the impact crater (Fig. 12b). The MOLA data also show a topographic plateau to the East of the impact crater with a surface dipping 1.2^o to the West. The fact that the crater

is situated on this slope explains that the lava flows buried only the western part of its ejecta (Fig. 12c).

Using the spatial resolution of 13 m/pixel, the pixel size periods (9, 7 and 4 pixels) are converted into meters (120, 90 and 50 m, respectively). Most geological units visible in the image are very well defined using the roughness map (Fig. 12d). They are divided into regions of interest (ROI) that we compare to a reference area, sampled in the plain located South of the crater and represented in the figure by the yellow polygon. At the extreme East, the very rough unit as compared to the reference corresponds to striated units of the Kasei valley floor. A portion of the crater's ejecta (blue ROI) appears very similar to the reference at 50 and 90 m, whereas it becomes rougher at the period of 120 m. The same observation is made for most ejecta deposits shown in Figure 9b. At this scale, the rough ejecta surface, inherited from the fragmentation and emplacement mechanism, seems not to be completely erased by smoothing coming from dust deposition and wind erosion. Lava flows (green ROI) display a very homogeneous roughness compared to the other units. Most of them are rougher than the reference (with significant roughness at the 50-m period), suggesting that the mantling by windblown sediments is too thin to hide the topography completely. This may result from the younger age of the lavas relative to the reference. Because the roughness is more important at 50 m than at 120 m, we suggest that the lavas are not composed of large blocks (several tens of meters large) but rather have a pattern at a few meters scale related to the cooling of typical fluid lavas. A very smooth area appears within the lava flows (red ROI). Even when "stretched" to the extreme, the HRSC image does not show the same pattern. Such a smooth area could indicate a roughness directly related to the lava flow (e.g., very fluid and smooth

pahoehoe-like lavas), or it could reflect a thick dust mantling.

We compared these results with the roughness determined by Kreslavsky and Head (2000). At the considered 0.6, 2.4 and 9.6 km scales, the roughness of the ejecta is systematically higher than that of the lava flow. Combining the two approaches, it appears that above a scale of about 50 m, the ejecta are systematically rougher than the lava flows, probably because the ejecta layer is partially, but not totally covered by dust. The dust coverage smoothed first the small spatial period. A part of the original ejecta is still visible at larger spatial period.

The examples outlined above suggest that: (i) the roughness map can be used to contribute to the mapping of geological units not otherwise seen in the original image, (ii) Martian crater ejecta is rougher than the lava flows in the studied area, implying that it is possible to distinguish roughness signatures which are not related to degradation processes.

4 Discussion and Conclusions

Our study provides a method for describing surface roughness at sub-hectometric scale linked to surface blocks and rock size distribution and organization. Somehow, it meets conclusions recently reached stating that: (i) careful spectral unmixing of HRSC images reveals that the shade-fraction images contain qualitative information on surface roughness at a subpixel scale (McCord et al. 2007); (ii) subpixel surface roughness variations can be quantified from HRSC by means of two-look approach techniques (Mushkin and Gillespie 2006, Mushkin and Gillespie 2005). The roughness variations derived from the

present work can be related to both the state of degradation (e.g., amount of dust mantling) and/or to its geological properties (e.g., lava flow type). Combining this information with other data (e.g., topography, high resolution images, thermal emission) and products (e.g., thermal inertia, macroscopic roughness, crater count) could be quite fruitful. Frequently, the thermal inertia calculated from THEMIS data is influenced by the upper few decimeters of the surface and allows for the distinction between rocky and dusty surfaces (Fergason et al. 2006). Our approach may detect and map the indurated dust that does not produce typical thermal signatures for fine particles. Such a combination will be useful for improving the description of the surface state and its physical modeling.

Moreover, a wide range of applications can be considered which may lead to a systematic analysis and classification of Martian surface roughness. This study is based on only a few examples, limiting the following conclusions, but demonstrates the potentially wide applications of the approach.

The roughness of impact crater ejecta often corresponds to degradation /deposition processes rather than roughness inherited by the impact process, and can be used to gain insight into these specific degradation processes and their timescales.

Regarding lava flows, an observed presence and diversity of roughness variations could be related either to different states of weathering lava or to various types of lava.

Regarding feature detection, the roughness map can be used for the mapping of geological units as well as sub-units not identified in the original image. Moreover, wrinkle ridges or fractures are highlighted by this algorithm and

could be used for a detailed regional mapping of such features, given the extended coverage of HRSC data.

Regarding age evaluation, variations in roughness of the ejecta may be used to determine the relative ages of various craters located in the same region. With the support of a few additional constraints provided by the regional geologic context, identical roughness associated with different crater ejecta may indicate the same state of degradation, suggesting identical formation times.

Regarding aeolian processes, the smoothing of a surface by dust deposition may be characterized by its roughness properties. Some wind streaks are not visible on the roughness map, implying a very thin accumulation, whereas other ones are detected, implying meters-thick accumulation of dust. Such a thickness suggests that wind streaks are features existing within the same pattern over geological times and under constant prevailing wind direction. The derivation of a surface ratio between wind streaks features that are only detectable from the albedo and features that are seen in the roughness map could be envisioned as a proxy for deriving quantitative estimates both on aeolian transport and depositional processes.

Acknowledgment

We thank the HRSC Experiment Teams at Freie Universitt Berlin and DLR Berlin, as well as the ESA Mars Express Project Teams at ESTEC and ESOC for the successful planning and acquisition of the imaging data as well as for making the processed data sets available. We acknowledge the

effort of the HRSC Co-Investigator Team members and their associates who have contributed to this investigation in the preparatory phase and in scientific discussions within the HRSC Team. For this study, the HRSC Experiment Team of the German Aerospace Center (DLR) in Berlin has provided map-projected HRSC image data, and standard HRSC Digital Elevation Models. This work was supported by an ESA post-doctoral fellowship attributed to A. Cord. The research has also benefited from support given by the French Space Agency CNES and by the PNP (Programme National de Plantologie) to the Co-Investigator French groups, respectively P.P. and D.B. at LDTP/UMR 5562/CNRS/ Toulouse University and P.M., N.M., and F.C. at IDES/UMR 8148/CNRS/Orsay-Paris Sud University. We gratefully thank Mikhail Kreslavsky, Alan Gillespie and the third anonymous reviewer for their constructive and thorough comments, which substantially improved this paper.

References

Adams, J. B., Gillespie, A. R., 2006. Remote Sensing of Landscapes with Spectral Images A Physical Modeling Approach. Cambridge University Press, Cambridge.

Aharonson, O., Zuber, M. T., Rothman, D., 2001. Statistics of Mars' topography from the Mars Orbiter Laser Altimeter. Journal of Geophysical Research 106, 23723 – 23735.

Balmino, G., 1993. The spectra of the topography of the Earth, Venus and Mars. Geophysical Research Letters 20 (11), 1063–1066.

Baratoux, D., Mangold, N., Pinet, P., Costard, F., 2005. Thermal properties of lobate ejecta in Syrtis Major, Mars: Implications for the mech-

anisms of formation. Journal of Geophysical Research 110, E04011, doi:10.1029/2004JE002314.

Barnouin-Jha, O. S., Schultz, P. H., 1996. Ejecta entrainment by impact-generated ring vortices : Theory and experiments. Journal of Geophysical Research 101 (E9), 21099–21115.

Beyer, R. A., McEwen, A. S., Kirk, R. L., Dec. 2003. Meter-scale slopes of candidate MER landing sites from point photoclinometry. Journal of Geophysical Research 108 (E12), doi:10.1029/2003JE002120.

Carr, M. H., Crumpler, L., Cutts, J., Greeley, R., Guest, J., Masursky, H., 1977. Martian impact craters and emplacement of ejecta by surface flow. Journal of Geophysical Research 82, 4055–4065.

Christensen, P., Moore, H., 1992. The Martian surface layer. In: Mars. University of Arizona Press, Tucson, pp. 686–729.

Christensen, P. R., Gorelick, N., Fergason, R., Dec. 2005. Searching for change in the Martian night: Investigating nighttime temperature anomalies using THEMIS. AGU Fall Meeting Abstracts, P24A–01.

Cord, A., Martin, P., Foing, B., Jaumann, R., Hauber, E., Hoffmann, H., Neukum, G., HRSC Co-Investigator team, 2005. Martian surface texture study by a filtering approach using Mars Express HRSC data. In: First Mars Express Conference. Noordwijk, The Netherlands, p. 138.

Cord, A., Pinet, P. C., Daydou, Y., Chevrel, S., 2003. Planetary regolith surface analogs: Optimized determination of Hapke parameters using multi-angular spectro-imaging laboratory data. Icarus 165, 414–427.

Costard, F., 1989. The spatial distribution of volatiles in the Martian hydrolithosphere. Earth, Moon and Planets 45, 265–290.

Dodds, P. S., Rothman, D., 2000. Scaling, universality, and geomorphology. Annual Review of Earth and Planetary Sciences 28, 571–610.

Fergason, R., Christensen, P., Kieffer, H. H., 2006. High-resolution thermal inertia derived from the Thermal Emission Imaging System (THEMIS): Thermal model and applications. Journal of Geophysical Research E12004 (111), doi:10.1029/2006JE002735.

Forsberg-Taylor, N. K., Howard, A. D., Craddock, R. A., 2004. Crater degradation in the Martian highlands: Morphometric analysis of the Sinus Sabaeus region and simulation modeling suggest fluvial processes. Journal of Geophysical Research 109, E05002, doi:10.1029/2004JE002242.

Garvin, J. B., Frawley, J. J., 2000. Global vertical roughness of Mars from Mars Orbiter Laser Altimeter pulsewidth measurements. In: Lunar and Planetary Science XXXI. Houston, Texas, p. 1884.

Golombek, M. P., Haldemann, A. F. C., Forsberg-Taylor, N. K., DiMaggio, E. N., Schroeder, R. D., Jakosky, B. M., Mellon, M. T., Matijevic, J. R., Oct. 2003. Rock size-frequency distributions on Mars and implications for Mars Exploration Rover landing safety and operations. Journal of Geophysical Research 108 (E12), 27–1.

Greeley, R., Ivsersen, J., 1985. Wind as a geological process. Cambridge Planetary Sciences series:4. Cambridge University Press.

Jain, A. K., Farrokhnia, F., 1991. Unsupervised texture segmentation using Gabor filters. Pattern Recognition 24(12), 1167–1186.

Jehl, A., 16 authors, HRSC Co-Investigator team, 2006. Improved surface photometric mapping across Gusev and Apollinaris from an HRSC/Mars Express integrated multi-orbit dataset: implication on Hapke parameters determination. In: Lunar and Planetary Science XXXVII. Houston, Texas, p. 1219.

Johnson, J., Grundy, W., Lemmon, M., Bell III, J., Johnson, M., Deen, R., Arvidson, R., Farrand, W., Guinness, E., Herkenhoff, K., Seelos IV, F.,

Soderblom, J., Squyres, S., 2006. Spectrophotometric properties of materials observed by Pancam on the Mars Exploration Rovers: 1. Spirit. Journal of Geophysical Research 111 (E02S14), doi:10.1029/2005JE002494.

Kirk, R. L., Barrett, J. M., Soderblom, L. A., 2003. Photoclinometry made simple? In: Working Group IV/9 , Workshop "Advances in Planetary Mapping 2003". Houston, Texas.

Kreslavsky, M., Bondarenko, N. V., Pinet, P. C., Raitala, J., Neukum, G., MEx-Co-I-team, 2006. Mapping of photometric anomalies of Martian surface with HRSC data. In: Lunar and Planetary Science XXXVII. Houston, Texas, p. 2211.

Kreslavsky, M. A., Head, J. W., 1999. Kilometer-scale slopes on Mars and their correlation with geologic units: Initial results from Mars Orbiter Laser Altimeter (MOLA) data. Journal of Geophysical Research 104, 21,911–21,924.

Kreslavsky, M. A., Head, J. W., 2000. Kilometer-scale roughness of Mars: Results from MOLA data analysis. Journal of Geophysical Research 105 (E11), 26,695–26,711.

McCord, T., Adams, J., Bellucci, G., Combes, J., Gillespie, A., Hansen, G., Hoffman, H., Jaumann, R., G., N., Pinet, P., Poulet, F., Stephan, K., Group, T. S. W., HRSC Co-Investigator team, 2007. The Mars Express High Resolution Stereo Camera spectrophotometric data : characteristics and science analysis. Journal of Geophysical Research in press.

Mushkin, A., Gillespie, A., 2005. Estimating subpixel surface roughness using remotely sensed stereoscopic data. Remote Sensing environment 99, 75–83.

Mushkin, A., Gillespie, A., 2006. Mapping sub-pixel surface roughness on Mars using high-resolution satellite image data. Geophysical Research Letters 33, L18204.1–L18204.6.

Mustard, J. F., Cooper, C. D., Rifkin, M. K., 2001. Evidence for recent climate

change on Mars from the identification of youthful near-surface ground ice. Nature 412, 411–414.

Neumann, G. A., Abshire, J. B., Aharonson, O., Garvin, J. B., Sun, X., Zuber, M. T., Jun. 2003. Mars Orbiter Laser Altimeter pulse width measurements and footprint-scale roughness. Geophysical Research Letter 30, 1561.

Orosei, R., Bianchi, R., Coradini, A., Espinasse, S., Federico, C., Ferriccioni, A., Gavrishin, A. I., Feb. 2003. Self-affine behavior of Martian topography at kilometer scale from Mars Orbiter Laser Altimeter data. Journal of Geophysical Research 108 (E4), doi:10.1029/2002JE001883.

Pelkey, S., Jakosky, B., Mellon, M. T., 2001. Thermal inertia of crater-related wind streaks on Mars. Journal of Geophysical Research 106 (E10), 23909–23920.

Pinet, P., 18-authors, HRSC and OMEGA Co-Investigator team, 2006. Mars Express /HRSC imaging photometry and MER Spirit / PANCAM in situ spectrophotometry within Gusev. In: Lunar and Planetary Science XXXVII. Houston, Texas, p. 1220.

Pinet, P., Cord, A., Chevrel, S., Daydou, Y., 2004. Optical response and surface physical properties of the Lunar regolith at Reiner Gamma formation from Clementine orbital photometry derivation of the Hapke parameters at local scale. In: Lunar and Planetary Science XXXV. Houston, Texas, p. 1660.

Pinet, P., Cord, A., Jehl, A., Daydou, Y., Chevrel, S., Baratoux, D., Greeley, R., Neukum, G., Bell, J. F., HRSC Co-Investigator team, MER/Athena-Science-Team, 2005a. Orbital imaging photometry and surface geologic processes within Gusev. In: EGU 05. Vienna, Austria, p. 9363.

Pinet, P., Cord, A., Jehl, A., Daydou, Y., Chevrel, S., Baratoux, D., Greeley, R., Williams, D., Neukum, G., HRSC Co-Investigator team, 2005b. Mars

Express imaging photometry and surface geologic processes at Mars: What can be monitored within Gusev crater? In: Lunar and Planetary Science XXXVI. Houston, Texas, p. 1721.

Pinet, P., Daydou, Y., Cord, A., Chevrel, S., Poulet, F., Erard, S., Bibring, J.-P., Y.Langevin, Melchiorri, R., Bellucci, G., Altieri, F., Arvidson, R., HRSC and OMEGA Co-Investigator team, 2005c. Derivation of Mars surface scattering properties from Omega spot pointing observations. In: Lunar and Planetary Science XXXVI. Houston, Texas, p. 1694.

Putzig, N. E., Mellon, M. T., Kretke, K. A., Arvidson, R. E., 2005. Global thermal inertia and surface properties of Mars from the MGS mapping mission. Icarus 173, 325–341.

Randen, T., Husoy, J., 1999. Filtering for texture classication: A comparative study. IEEE Transactions on Pattern Analysis and Machine Intelligence 21(4), 291–310.

Sagan, C., Toon, O., Gierash, P., 1973. Climate change on Mars. Science 181, 1045–1049.

Schultz, P., 1992. Atmospheric effects on ejecta emplacement. Journal of Geophysical Research 97, 13257–13302.

Schultz, P. H., Gault, D. E., 1979. Atmospheric effects on Martian ejecta emplacement. Journal of Geophysical Research 84 (B13), 7669–7687.

Scott, D., Tanaka, K., 1986. U.S.G.S. I Map 1802 A. In: XXII Lunar and Planetary Conference. Houston, Texas, pp. 865–866.

Seelos, F. P., Arvidson, R. E., Guinness, E. A., Wolff, M. J., 2005. Radiative transfer photometric analyses at the Mars Exploration Rover landing sites. In: Lunar and Planetary Science XXXVI. Houston, Texas, p. 2054.

Shkuratov, Y. G., Stankevich, D. G., Petrov, D. V., Pinet, P. C., Cord, A. M., Daydou, Y. H., Chevrel, S. D., 2005. Interpreting photometry of regolith-

like surfaces with different topographies: shadowing and multiple scattering. Icarus 173, 3–15.

Simpson, R., Harmon, J., Zisk, S., Thompson, T., Muhleman, D., 1992. Radar determination of Mars surface properties. In: Mars. University of Arizona Press, Tucson, pp. 652–684.

Tanaka, K., Scott, D., Greeley, R., 1992. Global stratigraphy. In: Mars. University of Arizona Press, Tucson, pp. 345–382.

Turcotte, D., 1987. A fractal interpretation of topography and geoid spectra on the Earth, Moon, Venus and Mars. Journal of Geophysical Research 92 (B4), E597–E601.

Weeks, R. J., Smith, M., Pak, K., Li, W.-H., Gillespie, A., Gustafson, B., 1996. Surface roughness, radar backscatter, and visible and near-infrared reflectance in Death Valley, California. Journal of Geophysical Research 101, 23077–23090.

Weszka, J. S., Dyer, C. R., Rosenfeld, A., 1976. A comparative study of texture measures for terrain classification. IEE Trans. Systems, Man, Cybernetics 6, 269–285.

Period	1	2	3
Texture	29 (19)	29 (18)	28 (17)
RMSS	12 (9)	11 (7)	12 (8)

Table 1

Mean value of the difference in percentage between the two overlapping textural images and the two overlapping RMSS images. Numbers in brackets correspond two standard deviations.

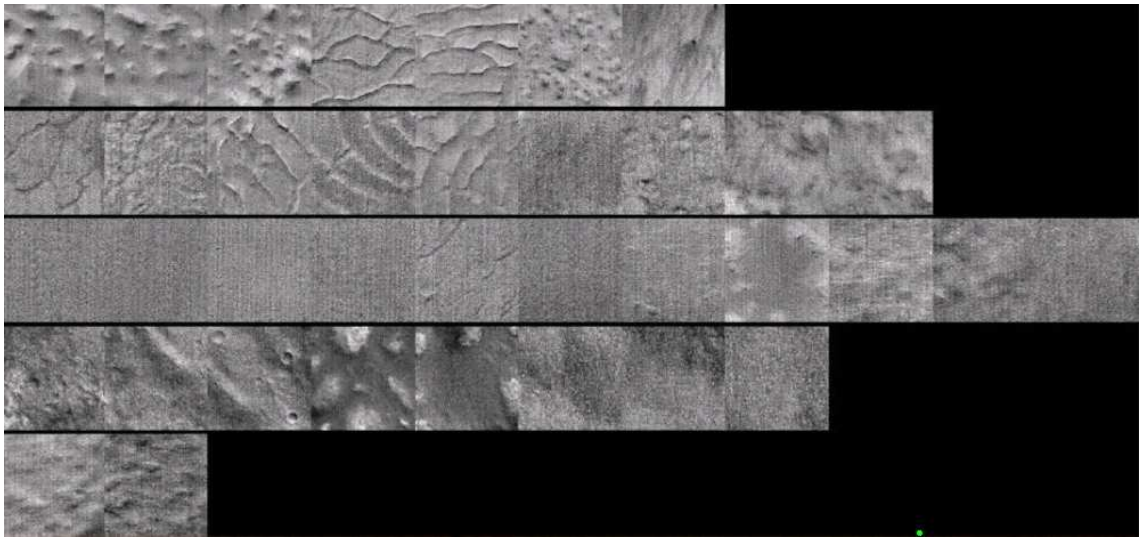

Fig. 1. Images extracted from the HRSC database exhibiting texture properties similar all along the image. Each line is a cluster corresponding to the best classification.

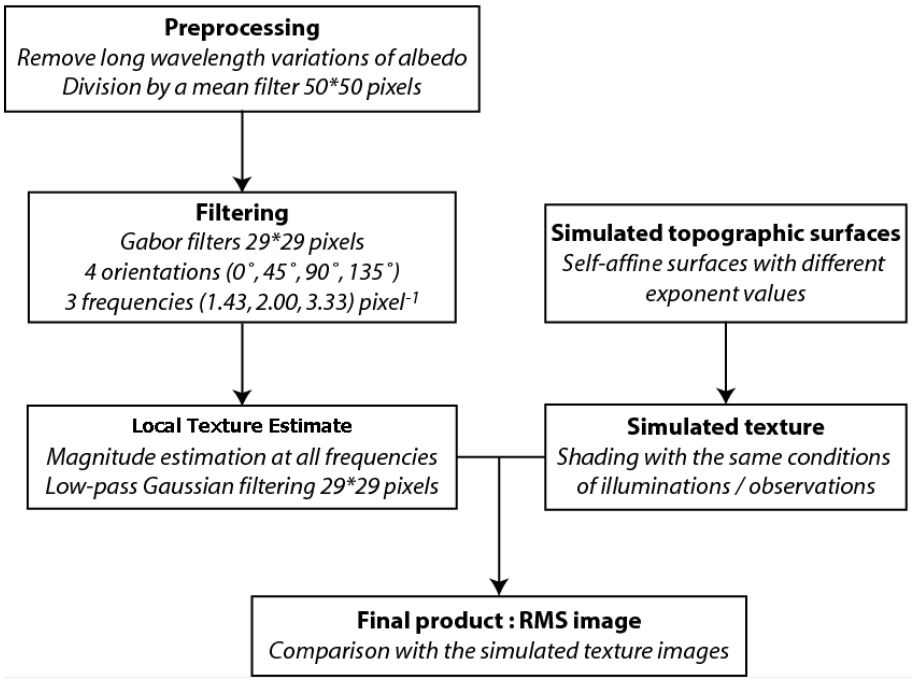

Fig. 2. Flow chart of the texture analysis method developed for roughness quantification of planetary surfaces.

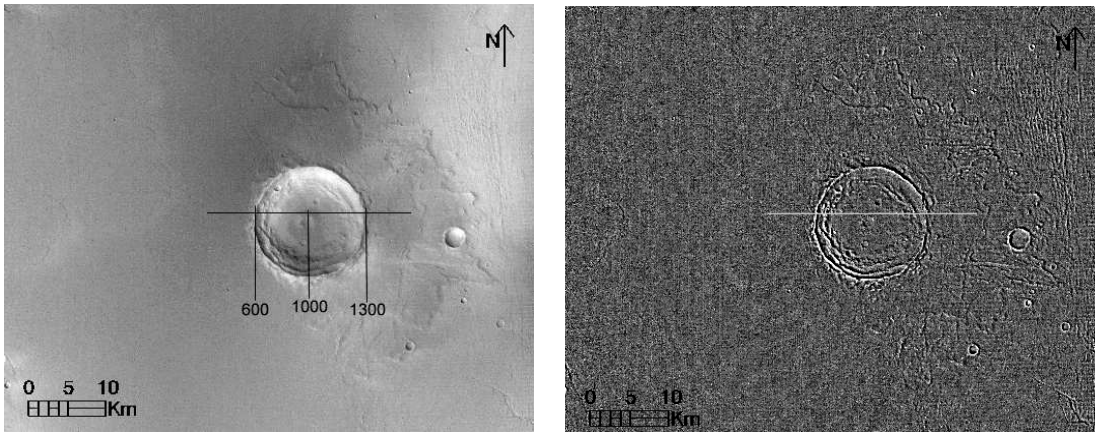

(a) (b)

Fig. 3. (a) Image from HRSC/Mars Express, orbit number 0071, nadir, with a spatial resolution of 13 m per pixel. Crater center at 16.3^o N, 280.8^o E. The horizontal black straight line corresponds to the profile presented in Figure 5. Pixel positions corresponding to crater center and rim (600, 1000 and 1300) are indicated. (b) Image obtained after preprocessing step.

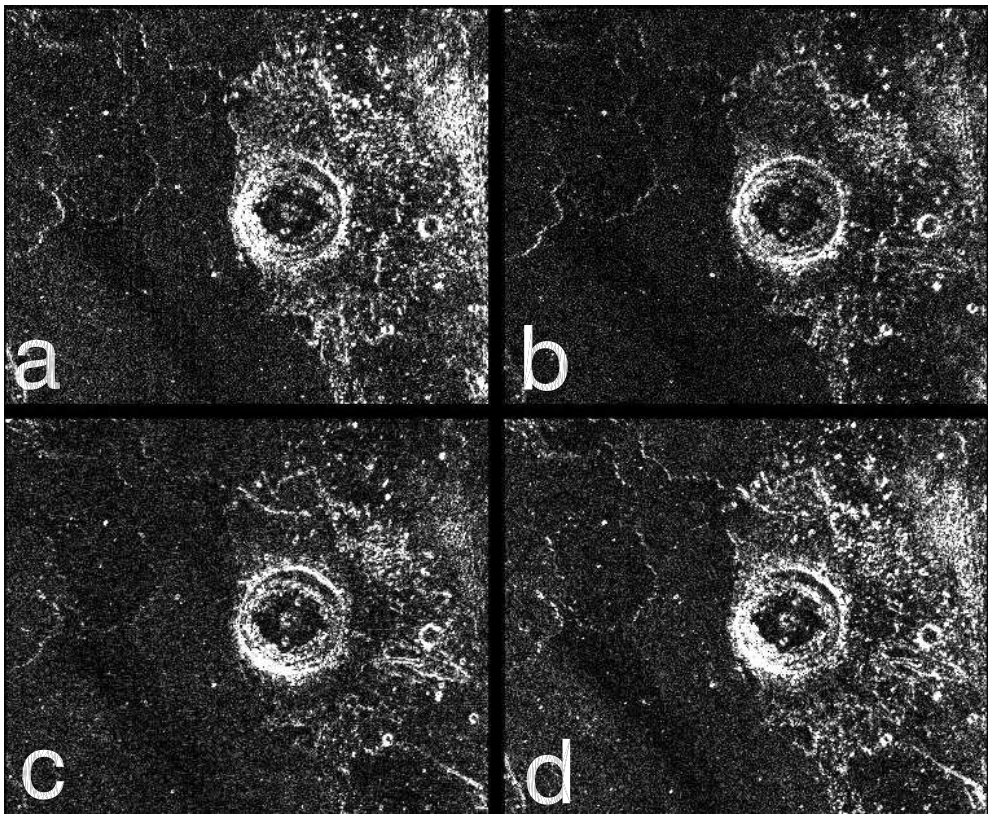

Fig. 4. Images obtained after filtering and magnitude computation. It shows the contribution of each orientation to the texture amount in white. The filter period is 7 pixel. The orientations from the horizontal are: (a) 0^o, (b) 45^o, (c) 90^o and (d) 135^o.

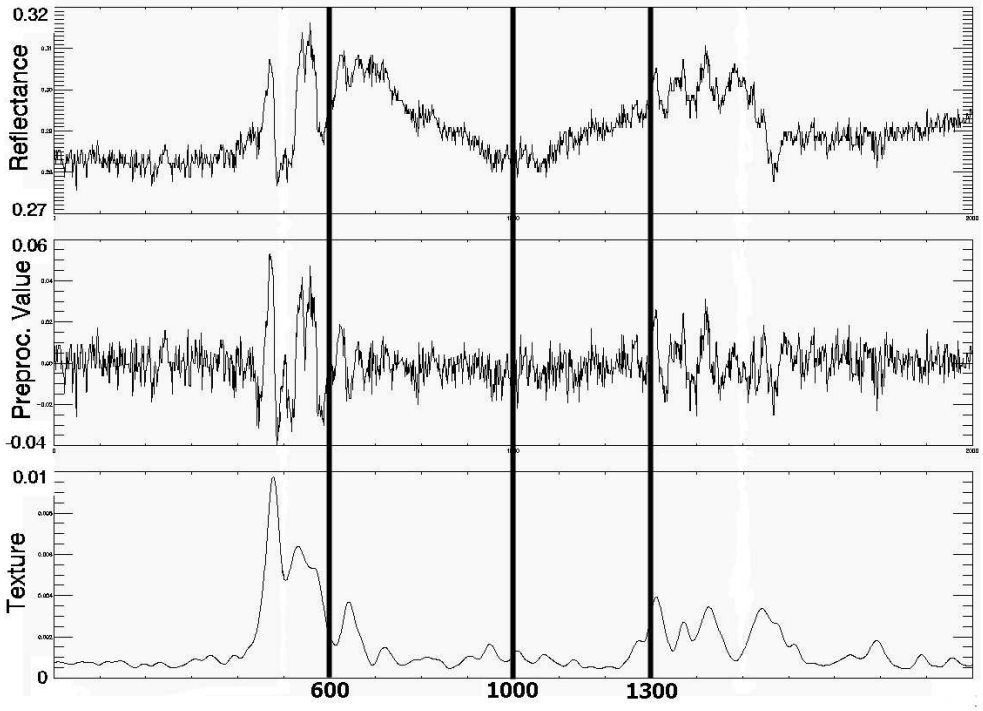

Fig. 5. Illustration of the preprocessing, filtering and local texture estimate steps of the process. Top: Reflectance profile of the original image according to the cross-section defined in Figure 3a. Middle: same profile after the preprocessing step. Bottom: same profile after the texture estimation. The pixels 600, 1000 and 1300 correspond to crater center and rim.

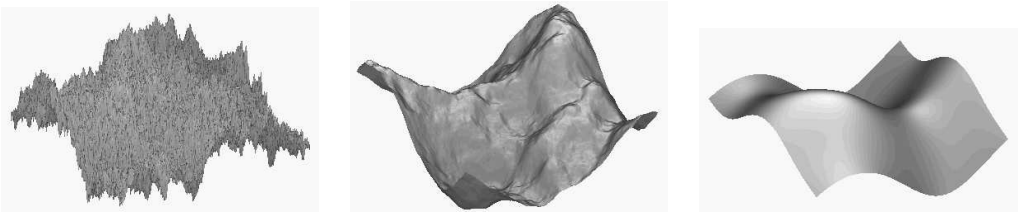

(a) (b) (c)

Fig. 6. Example of roughness images corresponding to simulated topographic surfaces with β values of 3 (a), 5 (b), and 9 (c). The incidence angle is 45^o in this example.

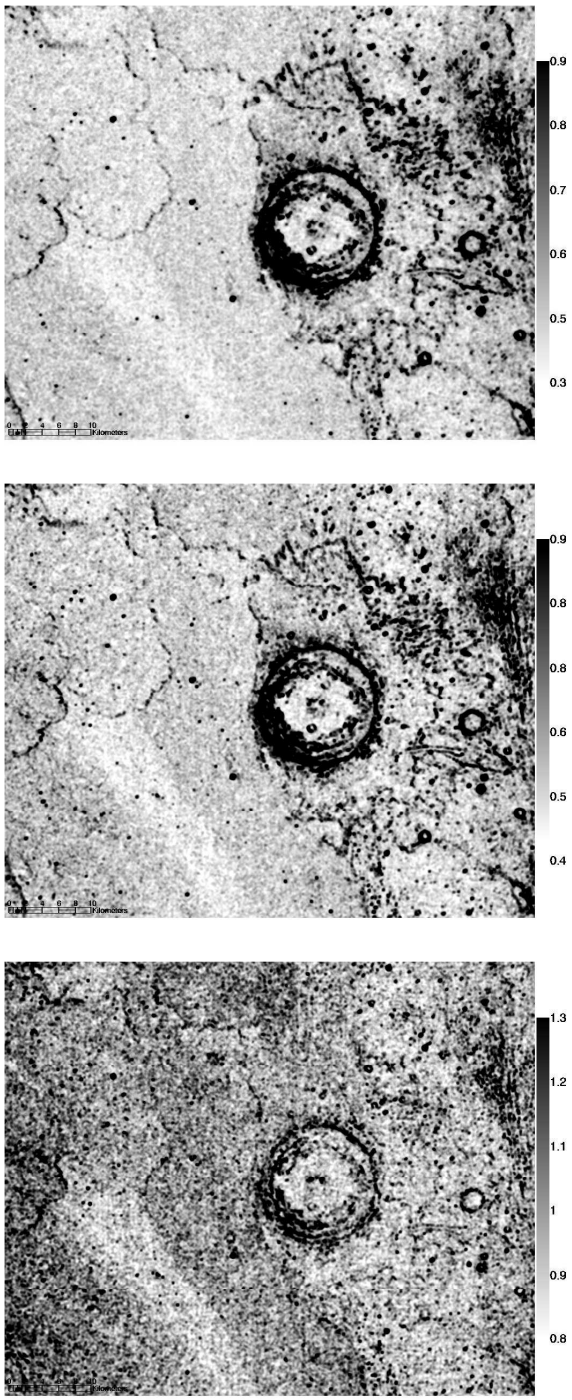

Fig. 7. Final outputs of the Gabor filtering process. From top to bottom, RMSS values for the periods corresponding to 9, 7 and 4 pixels respectively.

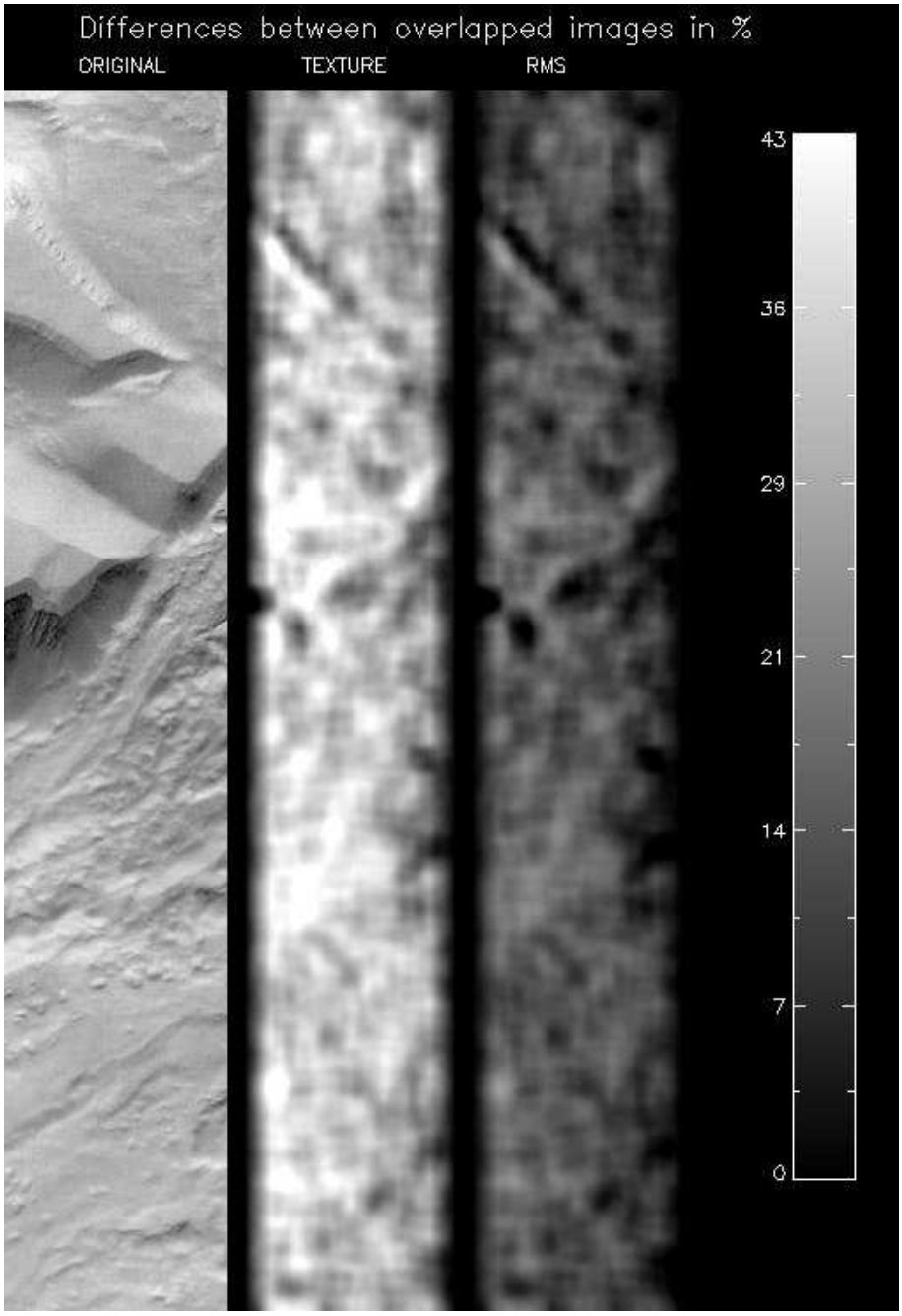

Fig. 8. From left to right: Image of the overlapped area, difference in percentage between the two textural images for the 7 pixel roughness scale and difference between the two RMSS images. The image size is 650 x 3550 pixels, and the spatial resolution 13m/pixel. The images are smoothed by a factor of 14 to minimize the effect of local misregistration. Grey-tone scale describes the image difference expressed in % for b and c.

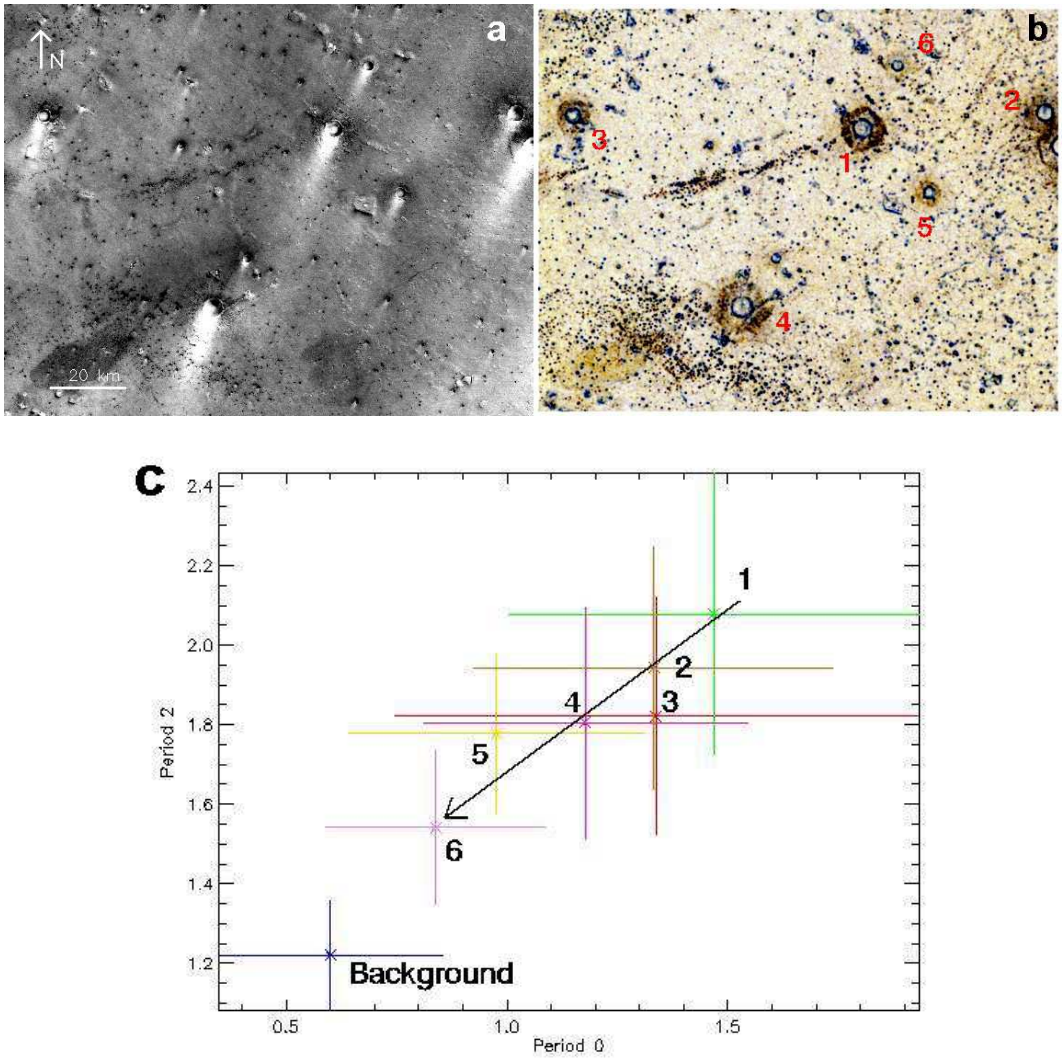

Fig. 9. (a) Image extracted from HRSC database (orbit 1436 $36^oN, 324^oE$) (b) RGB composite of the RMSS roughness values produced for the three roughness scales. Red, green, blue respectively correspond to 9, 7 and 4 pixels periods. The roughness increases from light to dark: the lighter the image, the smoother the surface. (c) 4 pixel period (X-axis) vs. 9 pixels period (Y-axis) RMSS values of crater ejecta. The error bars correspond to 3 standard deviations existing across the ejecta of each crater. The arrow goes from the roughest to the smoothest craters.

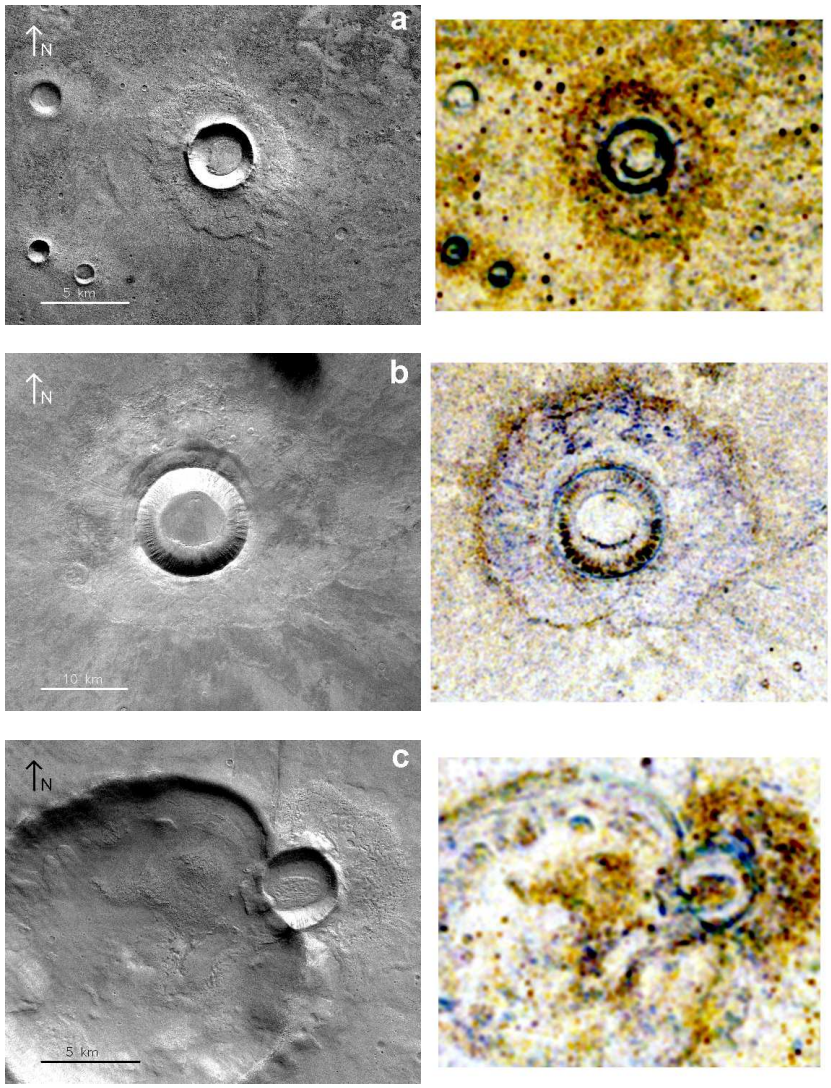

Fig. 10. Images extracted from HRSC database and associated RMSS images. Orbits and center coordinates are: (a) orbit 266 (-44.8^oN, 265^oE), (b) orbit 1354 (39.2^oN, 105.4^oE) and (c) orbit 279 (-45.2^oN, 264^oE). The color RMSS images are plotted using the same threshold as in Figure 9b and therefore are comparable.

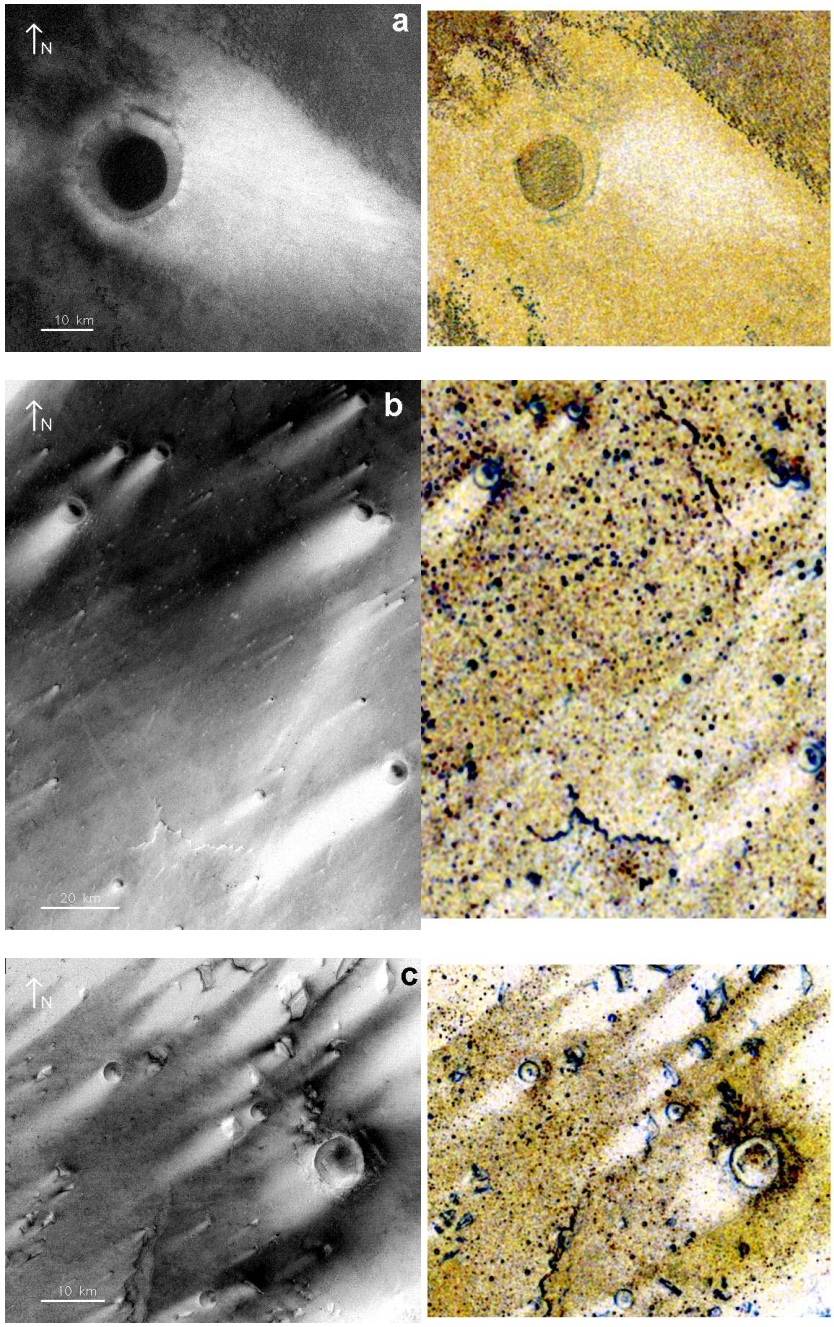

Fig. 11. Images extracted from HRSC database and associated RMSS images. Orbits and center coordinates are: (a) orbit 1425 (66.3^oN, 323.3^oE), (b) orbit 228 (14^oN, 158^oE) and (c) orbit 1152 (-13.5^oN, 161^oE). The color RMSS images are plotted using the same threshold as in Figure 9b and therefore are comparable.

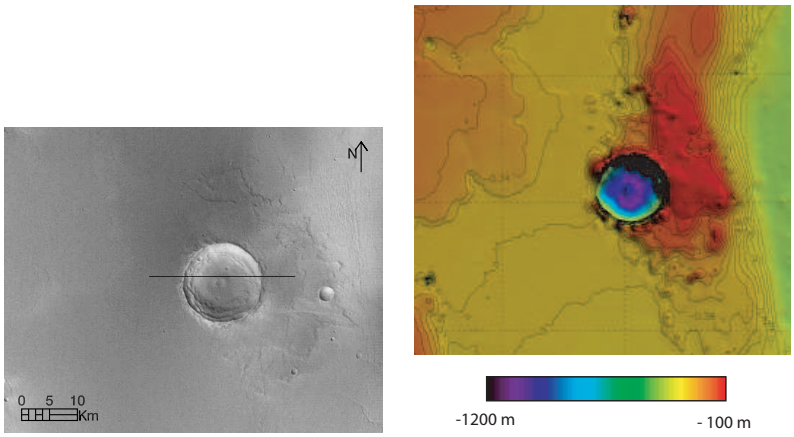

(a) (b)

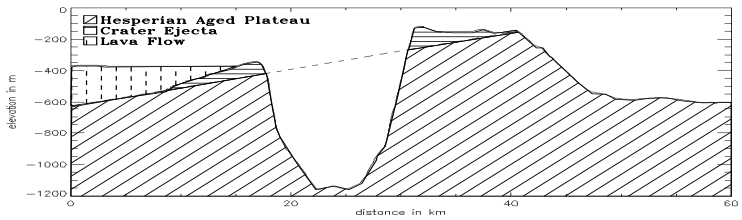

(c)

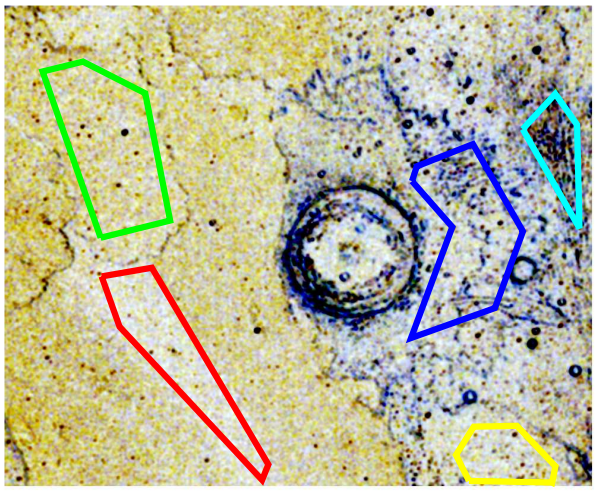

(d)

Fig. 12. (a) High-resolution (13m/pixel) image of the studied area, from HRSC image $h0071\_0000$. (b) Topography from MOLA data. (c) Simplified geological cross–section of the studied crater. The vertical exaggeration is 14. (d) RGB composite of the RMSS roughness values.